Novel nanostructure and magnetic properties of Co–Fe–Hf–O films

Nguyen Duy Ha[1], Manh-Huong Phan[2,4] and Chong Oh Kim[3]

[1] The Kamerlingh Onnes Laboratory, Leiden University, PO Box 9504, 2300 RA Leiden,
The Netherlands
[2] Advanced Composites Center for Innovation and Science, University of Bristol,
Queen's Building, University Walk, Bristol BS8 1TR, UK
[3] Research Center for Advanced Magnetic Materials, Chungnam National University,
Daejeon 305-764, Korea

E-mail: M.H.Phan@bristol.ac.uk

Abstract

The influence of the partial pressure of oxygen (P_{O_2}) on the microstructural and magnetic properties of sputtered Co–Fe–Hf–O films has been studied. It is shown that the films prepared under $P_{O_2} = 6\text{–}11.5\%$ with large saturation magnetization, $4\pi M_s \sim 18\text{–}21$ kG, large hard-axis anisotropy field, $H_{kH} \sim 30\text{–}84$ Oe, and high electrical resistivity, $\rho \sim 1400\text{–}3600$ $\mu\Omega$ cm, are excellent candidate materials for high-frequency applications of micromagnetic devices such as magnetic thin film inductors, transformers and thin film flux gate sensors. In particular, the good soft magnetic properties of $Co_{19.35}Fe_{53.28}Hf_{7.92}O_{19.35}$ nanocomposite films of 50–437 nm thickness, in addition to their high electrical resistivity, make them ideal for use in micromagnetic devices with an opening bandwidth of several gigahertz. This is attributed to the formation of a peculiar nanostructure in these samples. A strong magnetic phase separation appears to occur as the film thickness increases over 437 nm, which, in turn, modifies the high-frequency magnetic behaviour of the $Co_{19.35}Fe_{53.28}Hf_{7.92}O_{19.35}$ film.

(Some figures in this article are in colour only in the electronic version)

1. Introduction

Magnetic thin films are being widely used for a large number of technological applications, such as sensors and media for magnetic recording, automotive and aerospace industries, and are one of the most important tools for the preparation of multifunctional materials [1–7]. One of the key ingredients in the study of these material systems is understanding the correlation between their chemistry, structure and magnetic properties in order to design and produce novel thin films which meet the specific requirements of modern technologies [1, 7]. Therefore, considerable efforts have been devoted to clarifying the mechanism of film growth, the origin of magnetic couplings, spin transport across interfaces and spin–lattice interactions in magnetic thin films and nanostructures [2–9].

Recently there has been an emerging demand for the use of magnetic thin films in high-frequency applications including magnetic recording write-heads and soft underlayers for perpendicular media and thin film wireless inductor cores [6, 7, 10–19]. For these applications, magnetic thin films are required to have high electrical resistivity (ρ) to minimize energy loss due to eddy currents, and a large saturation magnetization ($4\pi M_s$) and hard-axis anisotropy field (H_{kH}) to increase the magnetic switching capacity at high frequencies [7, 10]. Although sputtered metallic films have long been used in magnetic storage applications, owing to their good high-density response and high saturation magnetization that enable the fast switching of high coercivity media, these materials are not desirable for use in devices working in the gigahertz regime [1–5]. This is because their electrical resistivity is relatively low, resulting in large energy losses due to eddy currents; in particular such a good high-frequency

[4] Author to whom any correspondence should be addressed.

magnetic response cannot be achieved in the GHz-frequency range [3–5].

In this context, the recent findings of new magnetic oxide thin films are of practical importance in high-frequency applications because these materials can show a good high-frequency performance into the gigahertz range owing to their resistivity, which is approximately ten times higher than that of conventional magnetic alloy films [6, 7, 10–19]. Hayakawa *et al* [10] first reported that Fe–M–O (M = Hf, Zr) magnetic films possessed a good magnetic softness owing to their nanostructure which consisted of ferromagnetic bcc nanocrystals (∼10 nm in size) embedded in an amorphous matrix containing large amounts of M and O elements. Soon after this work, several attempts were made to improve the high-frequency performance of these films [11–19]. It was found that the addition of Co to Fe–Hf–O films led to a significant improvement in the high-frequency magnetic response, mainly due to an increase in the crystalline anisotropy of the nanograins. Sato *et al* [11, 12] revealed that magnetic inductors using Co–Fe–Hf–O thin films had a higher quality factor and conversion efficiency than those using Fe–Hf–O and Co–Ta–Hf thin films. Since the Co–Fe–Hf–O thin films are insensitive to oxygen at interfaces, they could also be used as free layers for fabrication of spin-dependent tunnelling (SDT) junctions [16] and as electrode layers for tunnelling magnetoresistive (TMR) junction applications [17]. It was shown that the structure of a Co–Fe–Hf–O film consisted of α-Fe(Co)-rich bcc nanograins embedded in a HfO$_2$-rich amorphous matrix [10, 17, 19]. The highly resistive HfO$_2$-rich amorphous matrix contributed to the high resistivity of the film which significantly suppressed eddy current loss, and consequently gave rise to the good high-frequency performance [10–17]. The addition of large amounts of Hf and O was found to significantly increase the electrical resistivity of Co–Fe–Hf–O films but, in turn, deteriorate their magnetic softness [17, 18]. In order to produce such novel Co–Fe–Hf–O films (e.g. high ρ, large $4\pi M_s$ and H_{kH}), it is essential to tailor the microstructure of the film by varying the chemical composition.

The overall aim of the present work is to improve the high-frequency performance of Co–Fe–Hf–O films by fine-tuning the alloy composition with varying oxygen concentration, using the oxygen reactive rf-sputtering method. The results obtained indicate that the present films possess not only large saturation magnetization and a large hard-axis anisotropy field, but also high electrical resistivity. They are excellent candidate materials for application in micromagnetic devices working into the gigahertz regime.

2. Experimental details

Co–Fe–Hf–O films were deposited by reactive rf-sputtering using an Ar + O$_2$ atmosphere with a base pressure of less than 2.0×10^{-7} Torr, onto Si(100) substrates at ambient temperature, and in a dc magnetic field of 100 Oe to induce an in-plane uniaxial anisotropy. The films were fabricated from a composite target. Hf chips were placed very close to the outer plasma ring on the Co$_{30}$Fe$_{70}$ alloy target surface. The film samples were prepared with changes of partial pressure of oxygen ($P_{O_2} = 2$–13%). Then, the

$P_{O_2} = 11.5\%$ samples with a chemical composition of Co$_{19.35}$Fe$_{53.28}$Hf$_{7.92}$O$_{19.35}$ and thicknesses (t) varying from 50 to 2000 nm were fabricated in order to investigate influences of film thickness on the microstructure and magnetic properties of this film. The structure of all films prepared was examined by x-ray diffraction (XRD) and high-resolution transmission electron microscopy (TEM). The composition of the prepared films was analysed by Auger electron spectroscopy (AES) and Rutherford back-scattering spectroscopy (RBS). In addition, local micro-compositions were determined *in situ* by energy dispersive x-ray spectroscopy (EDS) plug-in modules of TEM. Magnetic hysteresis loops were measured using a vibrating sample magnetometer (VSM), along the easy and hard axes of magnetization. Note that the films were measured in a plane parallel (perpendicular) to the direction of the applied magnetic field. Electrical resistivity was measured by a standard four-probe method. Hard-axis magnetic permeability was measured using a permeameter in the frequency range of 0.1–10 GHz. Domain patterns of the films were observed using high-resolution magneto-optical Kerr microscopy.

3. Results and discussion

3.1. Structural analyses

First, the microstructure of all Co–Fe–Hf–O films was examined using XRD and TEM. The results are displayed in figures 1 and 2 for some representative samples. It can be seen from figure 1(a) that there is only a single peak around 43° for the film sample without oxygen ($P_{O_2} = 0$), indicating structural homogeneity, where the atoms are randomly arranged with a dominant Hf–Fe(Co) pair correlation [17]. In fact, when the sputtering is carried out in an Ar atmosphere ($P_{O_2} = 0\%$), the atmosphere preferentially reacts with Co and Hf forming clusters of Fe–Fe(Co) and Co$_2$Hf due to chemical phase separation [19]. This is verified by the TEM image (figure 2(a)) and the selected area diffraction (SAD) pattern (inset of figure 2(a)). Therefore, the single peak at 43° is α-Fe(Co)(110) in a mixture of Co$_2$Hf and Fe–Co amorphous matrix. As one can see from figure 1(a), the structure remains almost unchanged as the partial pressure of oxygen (P_{O_2}) increases up to 5% (see figure 1(a), for the $P_{O_2} = 0$–5% samples). This indicates that P_{O_2} has little influence on the microstructure of Co–Fe–Hf–O films in the range of 0–5%. This is also confirmed by the TEM images (not shown here). In contrast, the XRD patterns of the film samples with $6\% \leqslant P_{O_2} \leqslant 11.5\%$ (figure 1(a)) exhibit two main peaks around 32° and 45°, corresponding to HfO$_2$(111) and Fe–Co(110) lattice spacing. The broad (111) peak originates from the HfO$_2$-rich amorphous phase, while the sharp (110) peak belongs to the α-Fe(Co)-rich nanocrystalline phase [10]. This is verified by the TEM image (figure 2(b)) and SAD pattern (inset of figure 2(b)). In fact, when oxygen is present during sputtering, O preferentially combines with Hf, at sufficiently high concentration, forming a HfO$_2$-rich amorphous phase due to acquiring similar binding energies for metallic Hf and HfO$_2$. Therefore, the co-existence of the two different phases (i.e. the α-Fe(Co)(110) and HfO$_2$(111) phases) arises mainly from chemical phase separation occurring during film deposition, due to the difference in the oxygen affinities of Hf and Fe(Co). The TEM images (figures 2(b)
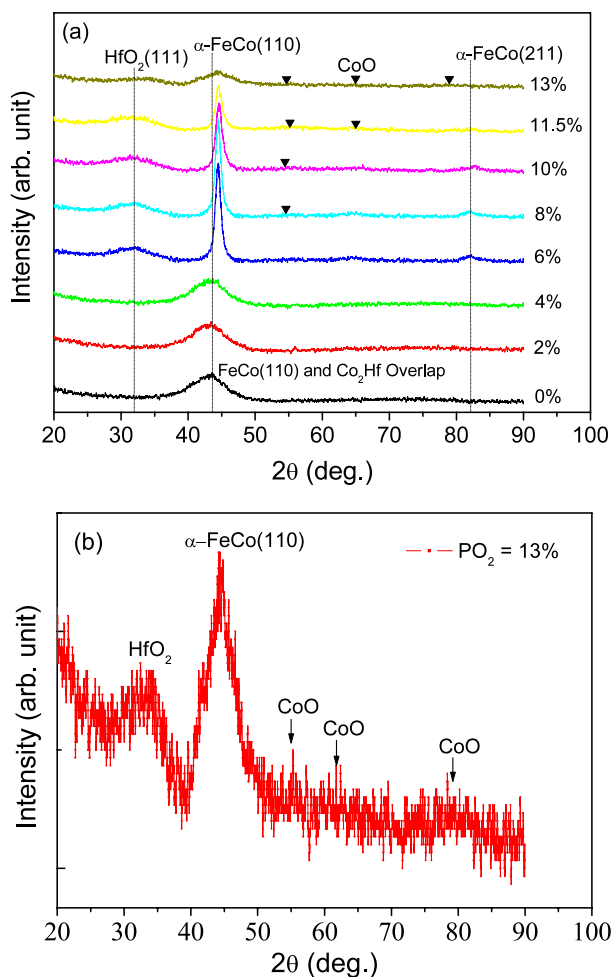
Figure 1. (a) XRD patterns of films with varying partial pressure of oxygen (P_{O_2}). (b) XRD pattern of the $P_{O_2} = 13\%$ sample as a clear example.

Figure 2. Cross-sectional TEM images and SAD patterns of the $P_{O_2} = 0\%$ sample (a) and the $P_{O_2} = 6\%$ sample (b), respectively. The circular symbols in (b) indicate centres at which the nanoparticles are formed and grow up. (c) In-plane TEM image of the $P_{O_2} = 11.5\%$ sample with arrows pointing to a preferentially anisotropic direction. The insets in (c) show a high-resolution in-plane TEM image with arrows pointing to a preferentially anisotropic direction (the upper inset) and a cross-sectional TEM image showing a laminate nanostructure (the lower inset), for the $P_{O_2} = 11.5\%$ sample.

and (c)) also indicate that the structure of the $6\% \leqslant P_{O_2} \leqslant 11.5\%$ samples contains α-Fe(Co)-rich bcc nanograins embedded in a HfO_2-rich amorphous matrix. It is worth noting from figure 1(a) that the peak of α-Fe(Co)(110) shifts from 43° for the $P_{O_2} < 6\%$ samples to 45° for the $6\% \leqslant P_{O_2} \leqslant 11.5\%$ samples, together with an increase in its intensity. This indicates changes in the composition and crystallinity. Moreover, the two peaks (i.e. the α-Fe(Co)(110) and HfO_2(111) peaks) shift slightly away from each other in the samples as P_{O_2} increases from 6 to 11.5%, indicating a stronger chemical phase separation in those samples with higher P_{O_2}. This is also verified by the TEM images (see figures 2(b) and (c)). Apart from the presence of the HfO_2-rich amorphous and α-Fe(Co)-rich nanocrystalline phases, the CoO magnetic oxide phase appears and develops in the samples with $P_{O_2} \geqslant 8\%$ (figure 1). This is verified by the SAD patterns (not shown here). It is found that the mean size of α-Fe(Co) grains, as determined from the Scherrer equation [20], decreases from 14 to 10 nm as P_{O_2} increases from 6 to 11.5%, respectively. The distribution of α-Fe(Co) nanograins becomes more uniform in those samples with higher P_{O_2} (see figures 2(b) and (c), for comparison). Interestingly, the optimal nanostructure is achieved in the sample with $P_{O_2} = 11.5\%$. For $P_{O_2} > 11.5\%$ sam-
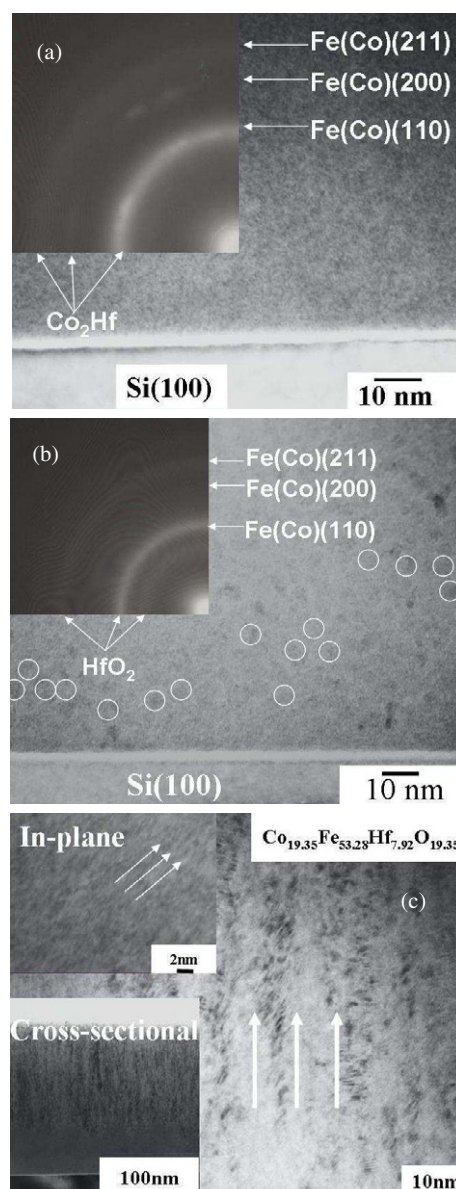
ples (e.g. the $P_{O_2} = 13\%$ sample), the peak HfO_2(111) shifts towards the side of the α-Fe(Co)(110) peak, which is much broader than that of the $6\% \leqslant P_{O_2} \leqslant 11.5\%$ samples (see figures 1(a) and (b)). In addition, there is a strong development of the CoO magnetic oxide phase in this sample (figure 1(b)). These findings indicate that the nanostructure is significantly modified in those samples with $P_{O_2} > 11.5\%$. The structural change of the $P_{O_2} = 13\%$ sample significantly modifies the magnetic properties, as shown later. It is interesting to note from figure 2(c) and its insets that the $P_{O_2} = 11.5\%$ sample
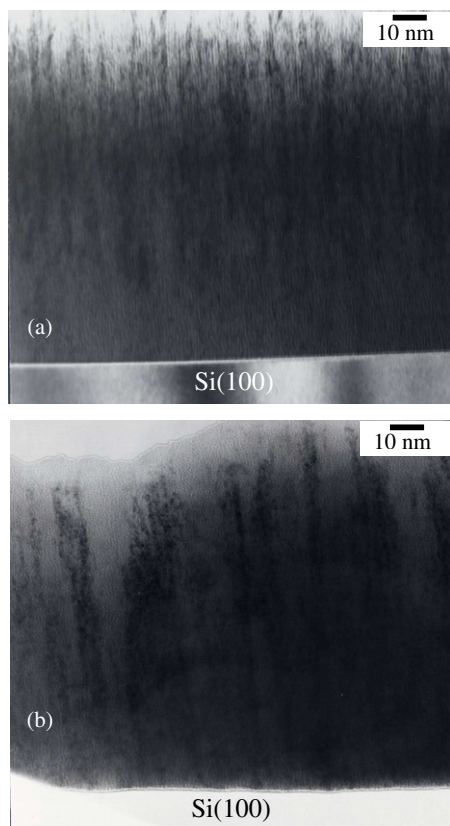
Figure 3. Cross-sectional TEM images of the $P_{O_2} = 11.5\%$ films with a thickness of 260 nm (a) and 890 nm (b).

Figure 4. (a) Magnetic hysteresis loops measured along the easy and hard directions for the $P_{O_2} = 11.5\%$ sample with a thickness of 432 nm. The inset shows the domain patterns subject to applied magnetic fields. (b) Frequency dependences of the real (μ') and imaginary (μ'') components of the relative permeability of this sample.

has a peculiar nanostructure which consists of nanocrystalline α-Fe(Co)-rich layers separated by amorphous HfO$_2$-rich layers. This nanostructure can be considered as a [Fe(Co)-rich/HfO$_2$-rich]$_n$ multilayer, where an exchange coupling of Fe–Fe(Co) takes place between two neighbouring ferromagnetic layers through an insulating HfO$_2$-rich amorphous layer [6, 7]. The laminate nanostructure of the $P_{O_2} = 11.5\%$ sample is believed to be the reason for its good magnetic properties.

In order to assess the structural growth mechanism for the $P_{O_2} = 11.5\%$ film, we investigated the influence of film thickness on the nanostructure of this sample using XRD and TEM. Results obtained from the XRD patterns reveal that when the film thickness increases the ratio of the HfO$_2$(111) and α-Fe(Co)(110) peak height increases, indicating the development of a HfO$_2$-rich amorphous phase at the expense of the α-Fe(Co)-rich nanocrystalline phase. This is consistent with what was reported in [10, 17, 19]. In the present case, a significant finding is that the HfO$_2$-rich amorphous phase becomes dominant over the α-Fe(Co)-rich nanocrystalline phase as the film thickness increases above 437 nm. The laminate nanostructure has only been observed in the $P_{O_2} = 11.5\%$ samples of thickness 50–437 nm. Increasing film thickness over 437 nm significantly modifies this nanostructure (see figures 3(a) and (b), for comparison) and hence the magnetic properties, as discussed below.
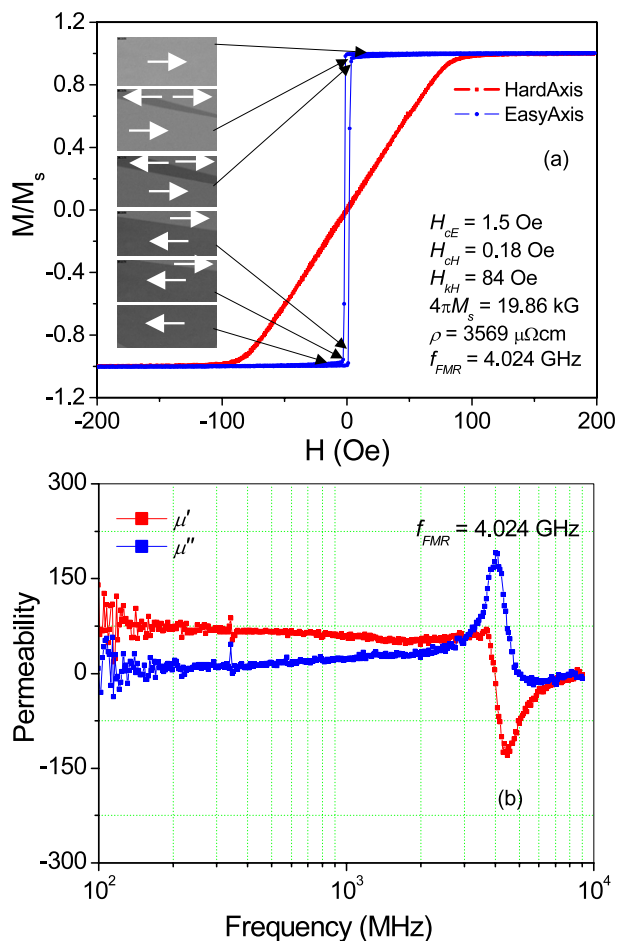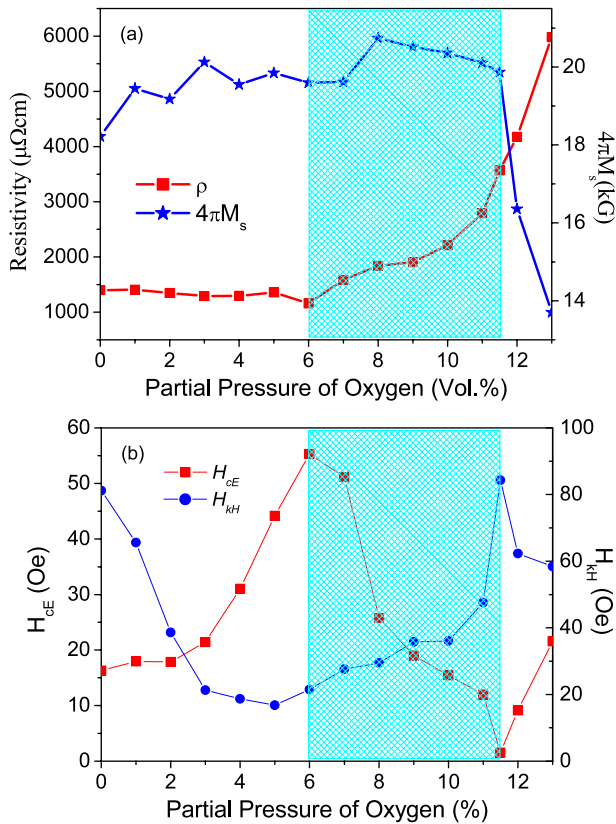
3.2. Magnetic and electrical properties

3.2.1. Effects of partial pressure of oxygen. The magnetic hysteresis loops along the easy and hard axes of the film samples were measured (see figure 4(a), for example, for the $P_{O_2} = 11.5\%$ sample) and the magnetic parameters extracted (e.g. saturation magnetization, $4\pi M_s$, easy-axis coercivity, H_{cE}, and hard-axis anisotropy field, H_{kH}) are plotted against partial pressure of oxygen (P_{O_2}) in figure 5. As one can clearly see from figure 4(a), the easy-axis hysteresis loop exhibits high coercive squareness, indicating that the magnetization reversal results mainly from irreversible domain wall motion across the film, whereas the magnetization reversal along the hard axis is caused by rotation of the domain magnetization [15]. This fully agrees with the changes in domain patterns upon application of a magnetic field (see the inset of figure 4(a)). It is obvious that for the case of the easy magnetization axis, the domain pattern remains essentially the same until the reversed field reaches the coercive field; it varies strongly at reversed fields which are close to the coercive field, accompanied by local switching of the image contrast of regions, and finally remains unchanged for higher reversed fields. Such an abrupt change in domain

Table 1. The magnetic and electrical parameters including the saturation magnetization, $4\pi M_s$, the hard-axis anisotropy field, H_{kH}, and the electrical resistivity, ρ, for several different magnetic thin films.

Composition	$4\pi M_s$ (kG)	H_{kH} (Oe)	ρ ($\mu\Omega$ cm)	Reference
$Fe_{61}Hf_{13}O_{26}$	13.00	7.5	500	[10]
$Co_{83}Ta_6Hf_{11}$	8.10	10.3	170	[10]
$Co_{44}Fe_{19}Hf_{15}O_{22}$	10.90	60.3	1700	[10]
$Co_{38.88}Fe_{50.02}Hf_{10.42}O_{0.68}$ ($P_{O_2} = 0\%$)	18.20	81.2	1401	Present work
$Co_{24.32}Fe_{50.43}Hf_{8.62}O_{16.64}$ ($P_{O_2} = 8\%$)	20.74	30.0	1839	Present work
$Co_{19.35}Fe_{53.28}Hf_{7.92}O_{19.35}$ ($P_{O_2} = 11.5\%$)	19.86	84.0	3569	Present work
$Co_{10.78}Fe_{60.59}Hf_{7.32}O_{21.3}$ ($P_{O_2} = 13\%$)	13.75	58.5	5979	Present work

Figure 5. (a) The dependences of the saturation magnetization ($4\pi M_s$) and electrical resistivity (ρ) on partial pressure of oxygen (P_{O_2}). (b) The dependences of the easy-axis coercivity (H_{cE}) and hard-axis anisotropy field (H_{kH}) on partial pressure of oxygen (P_{O_2}). The marked patterns indicate the optimal properties of the films for technological applications.

structure at about the coercive point is attributed to large-scale irreversible domain wall motion, which is linked to the easy-axis coercive squareness of the film as seen in figure 4(a).

Furthermore, it can be seen from figure 5(a) that with increasing P_{O_2} the electrical resistivity (ρ) remains almost constant for the $0\% \leqslant P_{O_2} < 6\%$ samples but starts to increase strongly for the $6\% \leqslant P_{O_2}$ samples. Meanwhile, the saturation magnetization ($4\pi M_s$) varies in a complex manner with increasing P_{O_2} up to 6%, then increases in the P_{O_2} range of 6–8%, and finally decreases for the $8\% < P_{O_2}$ samples (see figure 5(a)). On the increase in P_{O_2}, the easy-axis coercivity (H_{cE}) first increases in the P_{O_2} range of 0–6%, decreases in the P_{O_2} range of 6–11.5% and finally increases again for $P_{O_2} > 11.5\%$ (see figure 5(b)). In contrast to this, the hard-axis

anisotropy field (H_{kH}) first decreases with P_{O_2} up to 6%, then increases in the P_{O_2} range of 6–11.5% and finally decreases again for $P_{O_2} > 11.5\%$ (see figure 5(b)). The changes of the magnetic properties with P_{O_2} are likely to be related to the microstructural changes of the films.

It is interesting to emphasize from figure 5 (the marked patterns) that the $P_{O_2} = 6$–11.5% samples possess both larger saturation magnetization and electrical resistivity than the $P_{O_2} = 0\%$ sample. The large hard-axis anisotropy field (H_{kH}) and small easy-axis coercivity (H_{cE}) values are also achieved in these samples. For comparison, table 1 summarizes the important parameters of several films that are good candidate materials for magnetic recording and sensor applications. Obviously, the present films exhibit superior properties to the comparison films (table 1) and other films reported in the literature [10–19]. Among them, the $P_{O_2} = 11.5\%$ sample ($Co_{19.35}Fe_{53.28}Hf_{7.92}O_{19.35}$) exhibits the softest magnetic properties ($4\pi M_s = 19.86$ kG and $H_{cE} = 1.5$ Oe) together with a high electrical resistivity ($\rho = 3569$ $\mu\Omega$ cm). In addition, this film has the largest hard-axis anisotropy field, $H_{kH} = 84$ Oe. These give rise to an excellent high-frequency performance (see figure 4(b)). As can be seen in figure 4(b), the cut-off frequency of the real component of permeability (μ') reaches a value as high as ~3.7 GHz, which is much higher than those of Fe–Hf–O and Co–Ta–Hf films (~90 MHz) [10–12]. More interestingly, the imaginary component of permeability (μ'') remains constant up to $f = 3$ GHz and reaches a maximum at the ferromagnetic resonant frequency of $f_{FMR} = 4.024$ GHz. These enable micromagnetic devices to operate into the gigahertz range [10–17]. In relation to the electrical resistivity and magnetization data, the excellent high-frequency performance of the $P_{O_2} = 11.5\%$ sample can be attributed to its high electrical resistivity and to the large product of saturation magnetization and hard-axis anisotropy field (this relates to the high ferromagnetic resonance frequency of the film).

Now, let us discuss the possible origin of the good magnetic properties of the fabricated Co–Fe–Hf–O films. It is generally known that the magnetic moment of Co is larger in an amorphous Co-based alloy than in its corresponding crystalline counterpart and so Co_2Hf clusters in the galaxy of Co–Co(Fe) clusters can contribute to the high values of $4\pi M_s$ (figure 5(a)). The appearance and growth of the HfO_2-rich amorphous phase causes an increase in H_{cE} as the P_{O_2} increases up to 6% (figure 5(b)). The decrease in H_{kH} with P_{O_2} in the range of 0–6% can be attributed to the decrease in the crystalline anisotropy [10]. The electrical resistivity seems independent of P_{O_2} for the $P_{O_2} < 6\%$ samples (figure 5(a)), revealing that P_{O_2} has a more pronounced influence on the magnetic properties

(e.g. $4\pi M_s$, H_{cE}, and H_{kH}) than the electrical properties (e.g. ρ). In contrast, for the $6\% \leqslant P_{O_2} \leqslant 11.5\%$ samples, since the HfO_2-rich amorphous phase becomes comparable with the α-Fe(Co)-rich crystalline phase, the nanostructures are formed with a desirable combination of these two phases. It is the formation of the α-Fe(Co)-rich nanocrystalline phase that causes a drop in H_{cE} for the $6\% \leqslant P_{O_2} \leqslant 11.5\%$ samples (figure 5(b)). Herein, the decrease of H_{cE} with P_{O_2} is due to the decrease in size of the α-Fe(Co) nanograins. The largest value of $4\pi M_s$ for the $P_{O_2} = 8\%$ sample can be attributed to the strongest enhanced atomic pair correlation of Fe–Fe(Co) due to oxygen-induced chemical phase separation. For the $8\% < P_{O_2}$ samples, it should be noted that the oxygen affinity went beyond Hf to combine with Co and converted part of it to magnetic CoO (see figures 1(a) and (b)). As a result, these samples contain high-moment metallic nanograins of α-Fe(Co) partially surrounded by antiferromagnetic CoO phases within an amorphous matrix dominated by HfO_2. The presence of CoO could weaken the exchange coupling of Fe–Fe(Co), thereby leading to a considerable reduction in $4\pi M_s$ with increasing P_{O_2}. In these samples, the CoO magnetic oxide also formed the basis for exchange coupling as well as providing a source for a preferential axis in the form of Co^{2+} ions. Since Co^{2+} ions possess large single-ion anisotropy, a small preferential occupation of these ions in octahedral sites with direction $\langle 111 \rangle$ can be a source for large anisotropy and hence for an increase in H_{kH} for the $P_{O_2} = 8$–11.5% samples. However, it alone cannot account for the strong increase in H_{kH} for the $P_{O_2} = 11.5\%$ sample. In this sample, the shape anisotropy may play a significant role [10, 14]. In other words, it is the formation of a laminate nanostructure that results in the largest value of H_{kH} ($\sim$84 Oe) and the smallest value of H_{cE} ($\sim$1.5 Oe). For $P_{O_2} > 11.5\%$ samples, the decrease of $4\pi M_s$ and the increase of H_{cE} arise mainly from the strong growth of an antiferromagnetic CoO phase and the weakened α-Fe(Co)-rich nanocrystalline phase due to the nanostructural change (figure 1(b)). It is therefore concluded that the presence of large amounts of O ($P_{O_2} > 11.5\%$) significantly modifies the nanostructure and hence the magnetic properties of the film.

The high values of resistivity of the Co–Fe–Hf–O films are attributed to the HfO_2-rich amorphous phase which is nonmagnetic and electrically insulating. The strong increase in ρ for the $P_{O_2} > 6\%$ samples arises mainly from the fact that the HfO_2-rich amorphous phase develops strongly and becomes dominant over the α-Fe(Co)-rich nanocrystalline phase.

3.2.2. Effects of film thickness. To further verify the formation of the peculiar nanostructure of the $Co_{19.35}Fe_{53.28}Hf_{7.92}O_{19.35}$ sample ($P_{O_2} = 11.5\%$) resulting in the softest magnetic properties, we have investigated the influences of film thickness on the nanostructure and magnetic properties of this sample. As noted above, the peculiar nanostructure has been observed only in the samples of thickness 50–437 nm. Increasing the film thickness over 437 nm significantly modifies the peculiar nanostructure (see figures 3(a) and (b)). It is the nanostructural change that significantly modifies the high-frequency magnetic behaviour. An example displayed in figure 6 is the frequency dependence of the relative permeability for the $P_{O_2} = 11.5\%$ films with varying thicknesses. As can be seen from figure 6, the cut-off frequency of
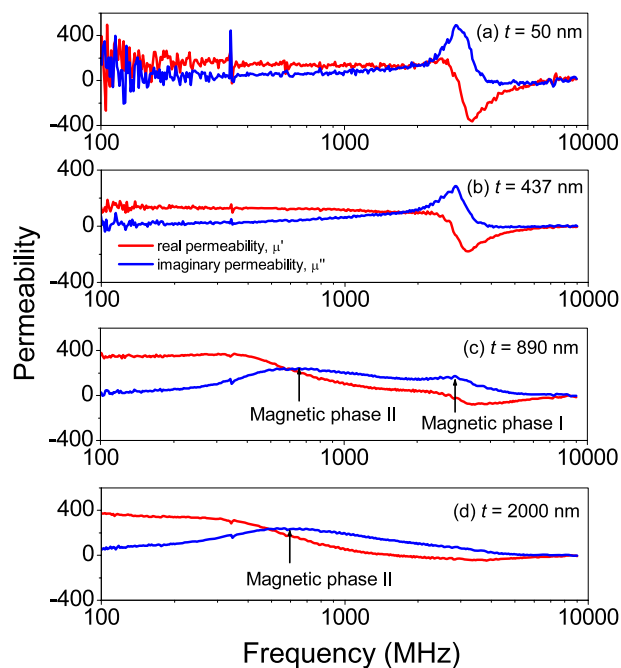
Figure 6. Frequency dependences of the real and imaginary components of relative permeability of the $P_{O_2} = 11.5\%$ sample with varying thickness. Phase I corresponds to the α-FeCo-rich nanocrystalline phase. Phase II corresponds to the HfO_2-rich amorphous phase.

the real component of permeability (μ') strongly decreases as the film thickness increases beyond 437 nm. Noticeably, the μ''–f curve shows a resonant single peak for thin films with $t \leqslant 437$ nm, whereas it has nearly double peaks for thicker films ($t > 437$ nm). Another remarkable feature is that the ferromagnetic resonant frequency (f_{FMR}) strongly shifts to lower values for $t > 437$ nm films. It reveals that a chemical phase separation between the α-Fe(Co)-rich nanocrystalline phase (phase I) and the HfO_2-rich amorphous phase (phase II) is significant as the film thickness increases over 437 nm. This agrees with the magnetization data (not shown here). With increasing film thickness, the HfO_2-rich amorphous phase becomes dominant over the α-Fe(Co)-rich nanocrystalline phase. This is consistent with the nanostructural changes as seen in the TEM images (figures 3(a) and (b)). Herein, the decreases of the cut-off frequency and the ferromagnetic resonant frequency (figure 6) are attributed to the strong decrease in the volume of the α-Fe(Co)-rich nanocrystalline phase. Meanwhile, the double-peak feature of the μ''–f curves (figure 6) is an indication of the strong phase separation occurring between the α-Fe(Co)-rich nanocrystalline phase and the HfO_2-rich amorphous phase. It is also noted from figure 6 that, when compared with thicker films ($t > 437$ nm), the appearance of much noisier signals in the μ–f curves for thinner films ($t < 437$ nm) in the frequency range of 1–500 MHz arises mainly from the presence of higher structural disorder in these films. This indicates that the degree of atomic order strongly depends on the preparation conditions (film thickness and deposition rate) [16]. In terms of these results, it is concluded that the formation of the laminate nanostructure in the $P_{O_2} = 11.5\%$ sample results in the excellent magnetic properties. Any change in the nanos-

tructure can result in significant variations in the magnetic nature of the film.

4. Conclusions

A detailed study has been performed of the structure and electrical and magnetic properties of Co–Fe–Hf–O magnetic thin films with varying partial pressure of oxygen ($P_{O_2} = 0$–13%). Excellent magnetic softness and high electrical resistivity are achieved in samples with $P_{O_2} = 6$–11.5%. The softest magnetic properties of the $P_{O_2} = 11.5\%$ sample are attributed to the formation of a laminate nanostructure. These films are strong candidate materials for high-frequency applications in micromagnetic devices, such as magnetic thin film inductors, transformers and thin film flux gate sensors. The change in partial pressure of oxygen and/or film thickness causes considerable variation in the nanostructure and magnetic properties.

Acknowledgments

References

[1] Howard J K 1986 *J. Vac. Sci. Technol.* A **4** 1

[2] Ohnuma M, Hono K, Onodera H, Onuma S, Fujimori H and Pedersen J S 2000 *J. Appl. Phys.* **87** 817

[3] Phan M H, Yu S C, Chung J S, Kim J S and Kim Y M 2003 *J. Appl. Phys.* **93** 9913

[4] Ha N D, Yoon T S, Kim H B, Lim J J, Kim C G and Kim C O 2005 *J. Magn. Magn. Mater.* **290/291** 1469

[5] Ha N D, Phan M H and Kim C O 2006 *J. Appl. Phys.* **99** 08F105

[6] Beach G S D and Berkowitz A E 2005 *IEEE Trans. Magn.* **41** 2043

[7] Beach G S D and Berkowitz A E 2005 *IEEE. Trans. Magn.* **41** 2053

[8] Skomski R 2003 *J. Phys.: Condens. Matter* **15** R841

[9] Srajer G 2006 *J. Magn. Magn. Mater.* **307** 1

[10] Hayakawa Y, Makino A, Fujimori H and Inoue A 1997 *J. Appl. Phys.* **81** 3747

[11] Sato T, Komai E, Yamasawa K, Morita S, Hatanai T and Makino A 1997 *IEEE Trans. Magn.* **33** 3310

[12] Sato T, Miura Y, Matsumura S, Yamasawa K, Morita S, Sasaki Y, Hatanai T and Makino A 1998 *J. Appl. Phys.* **83** 6658

[13] Yabukami S, Yamaguchi M, Arai K I, Watanable M, Itagaki A and Ando H 1999 *J. Appl. Phys.* **85** 5148

[14] Russek S E, Kabos P, Silva T, Mancoff F B, Wang D, Qian Z H and Daughton J M 2001 *IEEE Trans. Magn.* **37** 2248

[15] Lo C C H, Snyder J E, Leib J, Wang D, Qian Z, Daughton J M and Jiles D C 2001 *IEEE Trans Magn.* **37** 2337

[16] Wang D, Qian Z, Daughton J M, Nordman C, Tondra M, Reed D and Brownell D 2001 *J. Appl. Phys.* **89** 6754

[17] Esseling M, Luo Y and Samwer K 2004 *Europhy. Lett.* **68** 100

[18] Lee K E, Ha N D, Sun D S, Kollu P, Kim C G and Kim C O 2006 *J. Magn. Magn. Mater.* **304** e192

[19] Luo Y, Esseling M, Zhang K, Guntherodt G and Samwer K 2006 *Europhys. Lett.* **73** 415

[20] Cullity B D 1978 *Element of X-ray Diffraction* 2nd edn (Reading, MA: Addison-Wesley) p 102